2012 Biophysical Journal Volume 102 May 2012 2012–2021

Computational Analysis of the Regulation of EGFR by Protein Tyrosine Phosphatases

Calixte S. Monast,[†] Christopher M. Furcht,[†] and Matthew J. Lazzara[†‡*]
[†]Department of Chemical and Biomolecular Engineering and [‡]Department of Bioengineering, University of Pennsylvania, Philadelphia, Pennsylvania

ABSTRACT The tyrosine phosphorylated epidermal growth factor receptor (EGFR) initiates numerous cell signaling pathways. Although EGFR phosphorylation levels are ultimately determined by the balance of receptor kinase and protein tyrosine phosphatase (PTP) activities, the kinetics of EGFR dephosphorylation are not well understood. Previous models of EGFR signaling have generally neglected PTP activity or computed PTP activity by considering data that do not fully reveal the kinetics and compartmentalization of EGFR dephosphorylation. We developed a compartmentalized, mechanistic model to elucidate the kinetics of EGFR dephosphorylation and the coupling of this process to phosphorylation-dependent EGFR endocytosis. Model regression against data from HeLa cells for EGFR phosphorylation response to EGFR activation, PTP inhibition, and EGFR kinase inhibition led to the conclusion that EGFR dephosphorylation occurs at the plasma membrane and in the cell interior with a timescale that is smaller than that for ligand-mediated EGFR endocytosis. The model further predicted that sufficiently rapid dephosphorylation of EGFR at the plasma membrane could potentially impede EGFR endocytosis, consistent with recent experimental findings. Overall, our results suggest that PTPs regulate multiple receptor-level phenomena via their action at the plasma membrane and cell interior and point to new possibilities for targeting PTPs for modulation of EGFR dynamics.

INTRODUCTION

The binding of SH2- and PTB-domain-containing proteins to phosphorylated C-terminal tyrosines of the epidermal growth factor receptor (EGFR) links the receptor to cell-signaling pathways and to receptor trafficking mechanisms (1). Whereas the processes leading to EGFR tyrosine phosphorylation have been studied in detail, relatively little is known about quantitative aspects of receptor dephosphorylation by protein tyrosine phosphatases (PTPs) (2,3). Estimates of the rates of EGFR tyrosine dephosphorylation are limited (4–6), and the extent to which individual PTPs contribute to the net dephosphorylation kinetics of specific EGFR phosphotyrosines is unknown. The relative rates of EGFR tyrosine dephosphorylation at different cellular locations also remain poorly understood.

Beyond this fundamental knowledge gap, there are additional reasons why a quantitative understanding of EGFR tyrosine dephosphorylation is important. Indeed, dephosphorylation rates may influence receptor inhibition by targeted therapeutics (3), receptor trafficking (7), and downstream signaling (8). Tyrosine cycling between phosphorylated and unphosphorylated forms may also influence receptor sensitivity to noise (9), system responses to changes in ligand concentration (10), and sensitivity to changes in PTP and receptor concentrations (11). Of course, phosphatases play important roles in regulating signaling downstream of the receptor as well. In linear signaling cascades such as those associated with MAP kinases, phosphatases have a role in regulating signal induction, duration, amplification, and dampening (12).

A number of PTPs that regulate EGFR have been identified, including RPTPσ, RPTPκ, LAR, SHP-1, PTP1B, TCPTP, CDC25A, DEP-1, and LRP, with some information available on PTP localization. RPTPσ, RPTPκ, LAR, DEP-1, and LRP are anchored to the plasma membrane (13), whereas SHP-1 is present throughout the cytoplasm (14). PTP1B is tethered to the cytoplasmic side of the endoplasmic reticulum (15) and may be released into the cytoplasm (16), whereas TCPTP (16) and CDC25A (17) are shuttled between the nucleus and cytoplasm. Such spatial organization leads to important consequences for the dynamics of EGFR phosphotyrosine regulation by specific PTPs. For example, PTP1B dephosphorylates EGFR mainly after receptor endocytosis (18). In contrast, DEP-1's localization to the plasma membrane allows it to dephosphorylate EGFR before endocytosis in a process that may affect EGFR internalization (7).

The incomplete understanding of EGFR tyrosine dephosphorylation is reflected by the different ways this process has been incorporated into computational models of EGFR dynamics. One recent model simply assumed identical EGFR dephosphorylation rate constants for the plasma membrane and cell interior (5), while another included PTP effects without incorporating receptor trafficking (4). In previous models assuming that EGFR internalization is driven by ligand occupancy, neither phosphorylated species nor receptor dephosphorylation were explicitly included (19,20). In previous models of EGFR-mediated signaling focused on effects of receptor internalization on

Submitted June 1, 2011, and accepted for publication March 14, 2012.

*Correspondence: mlazzara@seas.upenn.edu

Editor: H. Steven Wiley.

0006-3495/12/05/2012/10 $2.00

doi: 10.1016/j.bpj.2012.03.037

downstream signaling (21) and network branching (22), dephosphorylation was omitted, presumably due to a focus on downstream dynamics. Another recent computational study concluded that ErbB receptors are mainly dephosphorylated in the cell interior (6). However, that model did not include explicit phosphorylation or dephosphorylation reactions; equated dimers with phosphorylated receptors; and assumed that dephosphorylation was equivalent to dimer uncoupling.

Here, we develop a mechanistic model to gain quantitative insight into the process of EGFR tyrosine dephosphorylation and its impact on other EGFR rate processes. The model consists of a set of coupled ordinary differential equations that describe the kinetics of EGFR phosphorylation, dephosphorylation, and trafficking. The model considers the dynamics of a single representative cytoplasmic EGFR tyrosine and accounts for the well-established coupling between receptor phosphorylation and endocytosis by requiring that receptors be phosphorylated for endocytosis to occur. Most parameters were taken from the literature or estimated using established methods. An additional aspect of our approach is fitting the four unknown parameters (including rate constants for EGFR tyrosine dephosphorylation at the plasma membrane and in the cell interior) to data gathered in HeLa cells for EGFR Y1068 phosphorylation response to EGFR activation by EGF, EGFR kinase inhibition, and PTP inhibition. These dynamic responses were quantified as percentages of phosphorylated EGFR using an immunoprecipitation-based method. Overall, our model results suggest that EGFR dephosphorylation occurs rapidly at the plasma membrane and in the cell interior in HeLa cells with a timescale that is smaller than that for EGF-mediated EGFR endocytosis. These dephosphorylation kinetics are predicted to exert control over EGFR endocytosis, EGFR inhibition, and phosphorylation sensitivity to changes in EGFR expression levels.

MATERIALS AND METHODS

Model development

General model considerations and topology

The model consists of a set of coupled ordinary differential equations that describe interactions of EGFR with itself (dimerization and phosphorylation), PTPs, EGF, ATP, and the EGFR kinase inhibitor gefitinib (Fig. 1 *A*). As these processes occur, EGFR is routed from the plasma membrane to an endosomal compartment where it is sorted for recycling or degradation (Fig. 1 *B*). Essential processes and model parameters are summarized in Fig. 1 and Table 1, respectively. The model includes 169 reactions, 52 species, and 25 parameters.

EGF binding, trafficking, and concentration

EGF binding at the plasma membrane and in the endosome was modeled as a reversible process characterized by rate constants for binding at pHs characteristic of these locations (23). EGF concentration was assumed to be constant in the extracellular space and time-dependent in the endosomal compartment.

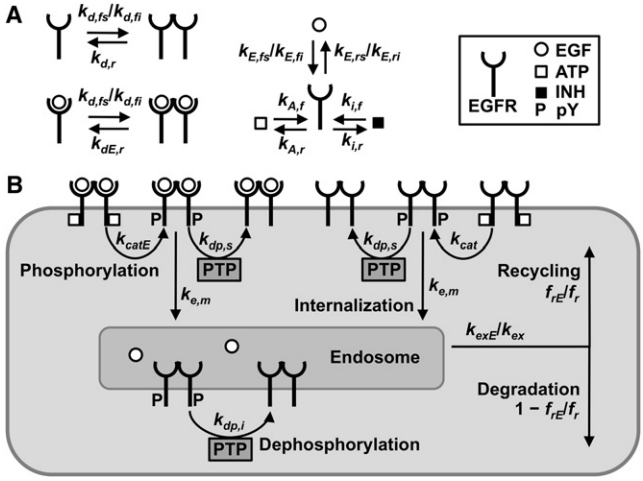

FIGURE 1 Model topology. (*A*) Binding processes include EGFR interactions with itself, EGF, ATP, and an EGFR kinase inhibitor (INH). (*B*) Additional processes include phosphorylation, dephosphorylation, and receptor trafficking.

ATP and inhibitor binding

Rate constants for ATP and gefitinib association with EGFR were estimated assuming diffusional limitations. Gefitinib was assumed to have a diffusivity of 2.5×10^{-6} cm$^2\cdot$s^{-1}, equal to that of ATP (24), and an interaction radius of 1 nm with EGFR (25). The rate constant for gefitinib dissociation was computed using its affinity for the EGFR kinase (26). The rate constant for ATP dissociation was estimated using an equilibrium-binding model and assuming that, for an ATP concentration of 1 mM (27), half of EGFR is inhibitor-bound at 21 nM gefitinib, consistent with experimental measurements (28).

EGFR dimerization

Rate constants for receptor dimerization were estimated assuming diffusional limitations (25), as in previous models (4,20). The diffusivity of EGFR was set to 1×10^{-10} cm$^2\cdot$s^{-1} (4), and the interaction radius was set to 1 nm (25). Cells and endosomes were approximated as spheres of radii 10 μm and 350 nm (29), respectively. Dimerization constant estimates were sensitive to changes in area but not to changes in EGFR levels. Thus, distinct dimerization rate constants were computed for the plasma membrane and endosome assuming 5×10^4 EGFR per compartment. Because EGF binding to EGFR promotes dimer formation (30), we defined dimer uncoupling rate constants for ligand-bound ($k_{dE,r}$) and ligand-free ($k_{d,r}$) EGFR, as in previous models (20,22). These constants were included in the parameter fit.

EGFR phosphorylation

EGFR phosphorylation was modeled as a process occurring within ATP-bound EGFR dimers during which both receptors are phosphorylated at a representative tyrosine. These reactions were characterized by rate constants for EGFR catalytic activity in the presence or absence of EGF (31). This structure allows for a small amount of EGFR phosphorylation in the absence of ligand, which has been observed even in the presence of a ligand-blocking antibody (32). The simplification of modeling EGFR phosphorylation at a single tyrosine residue has been used in previous EGFR models (e.g., (4,21)). Provided that the tyrosine considered plays a critical role in receptor endocytosis, this simplification should be acceptable for our purposes. Because the dynamics with which different EGFR

TABLE 1 Model parameters

Parameter	Description	Value	Source
$k_{E,fs}$ ($\mu M^{-1}\cdot min^{-1}$)	EGF binding to EGFR, forward, surface	6.3×10^{1}	(23)
$k_{E,rs}$ (min^{-1})	EGF binding to EGFR, reverse, surface	1.6×10^{-1}	(23)
$k_{E,fi}$ (endosome$\cdot min^{-1}$)	EGF binding to EGFR, forward, interior	3.9×10^{-4}	(23)
$k_{E,ri}$ (min^{-1})	EGF binding to EGFR, reverse, interior	6.6×10^{-1}	(23)
$k_{A,f}$ ($\mu M^{-1}\cdot min^{-1}$)	ATP binding to EGFR, forward	1.0×10^{5}	See text
$k_{A,r}$ (min^{-1})	ATP binding to EGFR, reverse	1.1×10^{7}	See text
$k_{i,f}$ ($\mu M^{-1}\cdot min^{-1}$)	Inhibitor binding to EGFR, forward	1.0×10^{5}	See text
$k_{i,r}$ (min^{-1})	Inhibitor binding to EGFR, reverse	2.1×10^{2}	See text
$k_{d,fs}$ (cell$\cdot min^{-1}$)	EGFR dimerization, forward, surface	6.7×10^{-4}	See text
$k_{d,fi}$ (endosome$\cdot min^{-1}$)	EGFR dimerization, forward, interior	1.1×10^{-2}	See text
$k_{d,r}$ (min^{-1})	EGFR dimerization, reverse, unoccupied	1.2×10^{4}	Fit
$k_{dE,r}$ (min^{-1})	EGFR dimerization, reverse, EGF-occupied	1.0×10^{-10}	Fit
k_{cat} (min^{-1})	Phosphorylation, unoccupied dimer	2.7×10^{0}	(31)
k_{catE} (min^{-1})	Phosphorylation, EGF-occupied dimer	1.3×10^{1}	(31)
$k_{dp,s}$ (min^{-1})	Dephosphorylation, surface	1.7×10^{0}	Fit
$k_{dp,i}$ (min^{-1})	Dephosphorylation, interior	1.5×10^{0}	Fit
S_E ($cell^{-1}\cdot min^{-1}$)	EGFR synthesis	Varies	See text
$k_{e,m}$ (min^{-1})	Phosphorylated EGFR internalization	Varies	See text
k_{exE} (min^{-1})	Endosomal exit, EGF-occupied	4.0×10^{-2}	(19)
k_{ex} (min^{-1})	Endosomal exit, unoccupied	4.0×10^{-2}	(19)
f_{rE}	Recycle fraction, EGF-occupied	0.5	(19)
f_r	Recycle fraction, unoccupied	0.8	(19)
ATP (μM)	Cellular ATP concentration	1.0×10^{3}	(27)
EGF (μM)	Extracellular EGF concentration	Varies	See text
INH (μM)	Inhibitor concentration	Varies	See text

tyrosines become phosphorylated (33) and dephosphorylated (28) appear to be roughly equivalent, the kinetics of tyrosine phosphorylation suggested by our model are likely representative of most EGFR tyrosines.

PTP activity

EGFR dephosphorylation was modeled as zeroth order with respect to PTPs, which obviates the need to specify PTP concentrations. To accommodate the possibility of different dephosphorylation rates at the plasma membrane and in the cell interior, we defined distinct parameters for these locations ($k_{dp,s}$ and $k_{dp,i}$, respectively), which were included in the parameter fit.

EGFR endocytosis and synthesis

Movement of phosphorylated EGFR from the plasma membrane to the cell interior (endocytosis) was modeled as a first-order process with a rate constant $k_{e,m}$. The specific endocytosis rate constant $k_{e,e}$ has been measured using ^{125}I-EGF, with $k_{e,e}$ computed as the slope of internalized ^{125}I-EGF counts versus the integral of surface-bound ^{125}I-EGF counts from $t = 0$ to the time of the measurement, for a series of times (34). A $k_{e,e}$ computed in this way is not generally interchangeable with the $k_{e,m}$ used in model rate equations describing endocytosis of phosphorylated species, even though the constants have similar units. This inconsistency arises because PTP activity at the plasma membrane results in at least some of the ligand-bound, membrane-localized receptors being unphosphorylated. In the limit of vanishing PTP activity at the membrane and rapid dimerization and phosphorylation, $k_{e,m} \rightarrow k_{e,e}$. To ensure that our results accurately reflected experimentally determined $k_{e,e}$ values, $k_{e,m}$ was iteratively determined for each simulation to achieve agreement between predicted internal and plasma membrane EGF dynamics and a $k_{e,e} = 0.13\ min^{-1}$ (35).

For our best-fit parameters (Table 1), $k_{e,m}$ was ~1.6-fold larger than $k_{e,e}$. Based on the discussion above, it is not surprising that the difference depends upon $k_{dp,s}$ (Fig. 2 *A*), with larger $k_{dp,s}$ values increasing the discrepancy between $k_{e,e}$ and $k_{e,m}$. The difference also depends upon EGFR expression because increased expression promotes dimerization and phosphorylation (Fig. 2 *B*). In Fig. 2, *A* and *B*, $k_{e,e}$ plateaus for arbitrarily large $k_{e,m}$ values as other processes become rate-limiting.

Because our model accounts for a small rate of EGFR degradation even in the absence of EGF, we incorporated an EGFR synthesis rate S_E to allow for steady initial EGFR levels. The S_E and $k_{e,m}$ values were determined iteratively before model calculations.

Endosomal exit and sorting

Receptor exit from the endosome was modeled using previously published parameters (19). The sorting of exiting species for degradation and recycling was modeled by assuming that constant fractions were routed to these pathways (19). EGFR sorting fractions were taken from measurements in mammary epithelial cells (19).

Parameter fitting

To determine the four unknown parameters, we began by fitting the model to data gathered from parental HeLa cells, including the phosphorylation

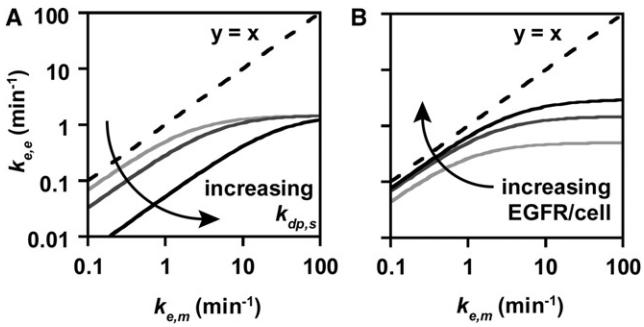

FIGURE 2 Relationship between model ($k_{e,m}$) and experimental ($k_{e,e}$) rate constants for EGFR endocytosis. The relationship between $k_{e,m}$ and $k_{e,e}$ was determined for 10 ng/mL EGF and (*A*) $k_{dp,s}$ = 1.7, 17, or 170 min^{-1} and (*B*) EGFR expression of 5×10^3, 5×10^4, or 5×10^5 $cell^{-1}$. For a given $k_{e,m}$, the S_E was computed and $k_{e,e}$ was calculated.

response of EGFR Y1068 to 1 and 10 ng/mL EGF, 100 μM pervanadate, and EGF-gefitinib pulse-chase (see Fig. S1). To refine our fits, we also included pulse-chase data from HeLa cells with conditional expression of dominant negative dynamin (HeLa.Dyn^{K44A}), which inhibits EGFR endocytosis (see Fig. S1). Measurements in cells with conditional expression of wild-type dynamin (HeLa.Dyn^{WT}) matched data from parental HeLa cells and were not included to avoid biasing the regression. Time-courses were restricted to $t \leq 20$ min to minimize potential effects of transcriptional regulation. Because our preliminary analysis revealed that data for the fraction of receptor phosphorylated would constrain parameter estimates more than data for relative changes in phosphorylation alone, we converted our immunoblot data to estimates of the percentage of EGFR phosphorylated at Y1068 (%pEGFR) using immunoprecipitation-based measurements (see Fig. S2), as described in the Supporting Material.

Parameter fitting was accomplished using simulated annealing to minimize the total error between model predictions and experimental data. For most data points, errors were computed as the square of the difference between model prediction and the experimental value divided by the magnitude of the experimental value. For pulse-chase data points, a similar form was used, except that experimental and model values were normalized to their values at 8 min post-EGF. This emphasized the fold-changes in pEGFR signals observed in the pulse-chase experiments. The error associated with each treatment (e.g., 1 ng/mL EGF) was computed as the sum of individual data point errors divided by the number of points for that condition, and the total error was computed as the sum of these treatment condition errors. The best-fit results are included in Table 1.

Sensitivity analysis

Model sensitivity to changes in parameters was computed by increasing and decreasing the values in Table 1 by factors of 2, 10, and 100. To compute raw measures of sensitivity, we summed the integrated differences between the base model and the two perturbed outputs over time. To compare different perturbation magnitudes, raw sensitivities for a given perturbation were reported as percentages of the maximum.

Model scope

To aid computational efficiency, our model topology assumed all dimer species to be symmetric (e.g., EGF binds both or neither EGFR monomers in a dimer). To test whether this simplification significantly affected our conclusions, we expanded the model to allow for asymmetric ligand binding. This increased the number of species from 52 to 119 and the number of reactions from 169 to 499, without changing the number of parameters. We refit the unknown parameters and found that $k_{dp,s}$ and $k_{dp,i}$ were nearly identical to the values found in the first fit (see Table S1 in the Supporting Material), although the dimer uncoupling constants changed to accommodate the increased number of species. All remaining calculations were based on the more compact model.

Representative HeLa cell

Unless otherwise noted, calculations reflect 5×10^4 EGFR/cell (36) and $k_{e,e} = 0.13$ min^{-1} (35). For HeLa.Dyn^{K44A} cells, calculations reflect $k_{e,e} = 0.01$ min^{-1} (35).

Model implementation

Codes were generated and compiled using the Systems Biology Toolbox 2 (SBT2) package for MATLAB (37) (The MathWorks, Natick, MA). The *simulannealbnd* function in the Global Optimization Toolbox was used to fit the model to experimental data.

Experimental methods

Using a combination of immunoprecipitation and immunoblotting, we generated quantitative estimates of %pEGFR in HeLa cells in response to treatment with EGF, pervanadate, or gefitinib for $t \leq 20$ min. These data were used to fit model parameters, as described above. Complete details on the experimental methods can be found in the Supporting Material.

RESULTS

EGFR phosphorylation dynamics in HeLa cells

Experimental measurements of %pEGFR for 20 min treatment with 1 ng/mL EGF, 4 min treatment with 10 ng/mL EGF, and 20 min treatment with 100 μM pervanadate were 11.6 $\pm$ 0.7%, 35.7 $\pm$ 6.8%, and 13.1 $\pm$ 2.7%, respectively. As described in the Supporting Material, these measurements were used to convert immunoblot data to estimates of %pEGFR for all time points (Fig. 3).

Treatment of parental HeLa cells with EGF or pervanadate resulted in time-dependent induction of EGFR Y1068

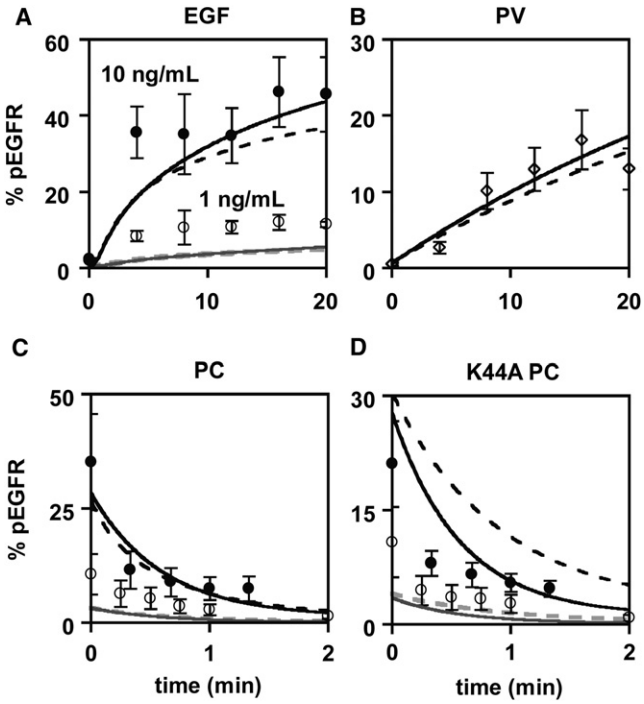

FIGURE 3 Model recapitulation of experimental EGFR phosphorylation measurements. The percentage of EGFR phosphorylated at Y1068 (%pEGFR) was measured for several experimental conditions using the approaches outlined in the Supporting Material. Data are represented as averages $\pm$ SE and were fit to determine four parameters, as described in the Materials and Methods. Measurements and model calculations were made for: (*A*) 1 or 10 ng/mL EGF treatment of parental HeLa cells; (*B*) 100 μM pervanadate (*PV*) treatment of parental HeLa cells (simulated by setting $k_{dp,s} = k_{dp,i} = 0$ min^{-1}); (*C*) 8 min treatment with 1 or 10 ng/mL EGF followed by 4 μM gefitinib (pulse-chase; PC) of parental HeLa cells; and (*D*) pulse-chase conditions as in panel *C* in HeLa.Dyn^{K44A} cells ($k_{e,e} =$ 0.01 min^{-1} (35)). Note that, in panels *C* and *D*, $t = 0$ min corresponds to the time when the gefitinib chase was added to cells. (*Dashed lines*) Model results generated using parameters from a fit to parental HeLa data only (*A–C*); (*solid lines*) model results generated using parameters from a fit to all data (*A–D*). Model and experimental results for 1 ng/mL EGF (*gray lines/open circles*); 10 ng/mL EGF (*black lines/solid circles*); and PV (*black lines/open diamonds*).

phosphorylation (Fig. 3, *A* and *B*, and Fig. S1), with estimated %pEGFR values as high as ~45% for a 20-min treatment with 10 ng/mL EGF. In response to pervanadate, %pEGFR levels rose as high as ~15%, an effect that is qualitatively consistent with previous results (e.g., Offterdinger et al. (38)). When parental cells were treated for 8 min with 1 or 10 ng/mL EGF and then treated with 4 μM gefitinib, pEGFR levels returned to baseline levels within ~1 min after gefitinib addition (Fig. 3 *C* and see Fig. S1). Similar trends in EGFR phosphorylation dynamics for such pulse-chase experiments have been previously reported (e.g., Offterdinger et al. (38)). To directly probe EGFR dephosphorylation at the plasma membrane, pulse-chase experiments were also performed in HeLa.Dyn^{K44A} cells. Even with impaired EGFR endocytosis, EGFR was dephosphorylated within ~1 min after gefitinib addition (Fig. 3 *D* and see Fig. S1).

Model fitting to experimental data

Parameter fitting revealed that data from parental HeLa cells only were best recapitulated when $k_{dp,i}$ and $k_{dp,s}$ were of similar magnitudes, with $k_{dp,i} > k_{dp,s}$ (see Table S2, entry for *K44A PC removed*). Even though $k_{dp,i}$ was larger than $k_{dp,s}$, the magnitude of $k_{dp,s}$ suggests significant regulation of EGFR by PTPs at the plasma membrane. The fit results also suggest a difference in $k_{dE,r}$ and $k_{d,r}$ which is larger than previously reported (20,22), which is a consequence of topological differences between our model and previous models. Using these fitted parameters, the model recapitulated the EGFR phosphorylation data in parental cells reasonably well (Fig. 3, *A–C*, *dashed lines*). Response to pervanadate was well captured by the model, and, with the exception of the response to 10 ng/mL EGF at 4 min, recapitulation of data for 10 ng/mL EGF (ligand-only and pulse-chase) was also generally good. The largest discrepancies between model and experiment were observed for ligand-only and pulse-chase kinetics for 1 ng/mL EGF, with the model underestimating the former and overestimating the latter. Thus, the model could not completely reconcile the best-fit PTP kinetics with the modest induction of EGFR phosphorylation for 1 ng/mL EGF.

Using parameters from fitting parental data only, the model predicted that EGFR dephosphorylation would occur within ~2 min in pulse-chase experiments in HeLa.Dyn^{K44A} cells, which is slower than the rate observed experimentally (Fig. 3 *D*). To refine our parameters, we refit the model to data including the HeLa.Dyn^{K44A} pulse-chase data. Doing this, $k_{dp,s}$ increased to a value slightly larger than $k_{dp,i}$ (Table 1) and model agreement with HeLa.Dyn^{K44A} pulse-chase data improved (Fig. 3 *D*, *solid black line*) without altering recapitulation of data from parental HeLas (Fig. 3, *A–C*, *solid lines*). All remaining calculations use the refined model parameters (Table 1).

Variations in the fit results among replicate fits led to negligible variation in model output. Thus, we reported parameters for the lowest error among fits for given conditions.

Contributions of specific data and topological features to fitting results

We further explored the fit results by examining variation in the total model error and errors for individual experimental conditions for variations in $k_{dp,s}$ and $k_{dp,i}$. The other two fitted parameters were left as listed in Table 1 because the model was relatively insensitive to changes in these (see Fig. S3).

As expected, added consideration of the HeLa.Dyn^{K44A} pulse-chase data tightened the domain in $k_{dp,s}/k_{dp,i}$ parameter space in which the total error was minimized (Fig. 4, *A* and *B*). Agreement with data for response to EGF alone was best for a $k_{dp,i}$ which was lower than that found by regression against the complete data set (Fig. 4 *C*), whereas agreement with pulse-chase data was best for a $k_{dp,i}$ which was larger than that found by regression against all data

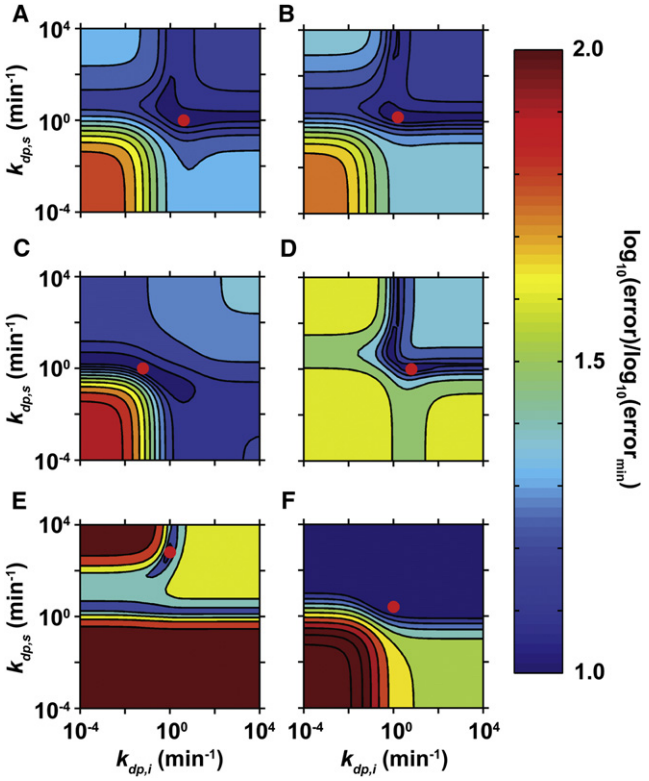

FIGURE 4 Effect of variation in surface ($k_{dp,s}$) and interior ($k_{dp,i}$) dephosphorylation rate constants on model agreement with EGFR phosphorylation measurements. Model error was calculated for ranges of $k_{dp,s}$ and $k_{dp,i}$ considering: (*A*) all data from parental HeLa cells, (*B*) all data from parental and HeLa.Dyn^{K44A} cells, (*C*) EGF treatment in parental HeLa cells only, (*D*) EGF-gefitinib pulse-chase experiments in parental HeLa cells only, (*E*) EGF-gefitinib pulse-chase experiments in HeLa.Dyn^{K44A} cells only, and (*F*) pervanadate treatment in parental HeLa cells only. For these calculations, $k_{dp,s}$ and $k_{dp,i}$ were set before computing $k_{e,e}$ and S_E. (*Red circles*) Error minima. To compare different plots on an equal basis, the scale was defined as the log of the error divided by the log of the global error minimum.

(Fig. 4 *D*). Not surprisingly, optimal model agreement with HeLa.Dyn^{K44A} cell pulse-chase data alone required a $k_{dp,s}$ larger than that found for regression against all data (Fig. 4 *E*). Interestingly, the HeLa.Dyn^{K44A} cell pulse-chase data also constrained $k_{dp,i}$ tightly, because these data include an initial 8 min response to EGF alone. Optimal model agreement with data from pervanadate (Fig. 4 *F*) was achieved for $k_{dp,s}$ ~10^0 min^{-1} and higher, resulting from a need to explain increased receptor phosphorylation when receptors were mainly at the cell surface. Interestingly, all data considered tended to push $k_{dp,s}$ to nonnegligible values. It may seem somewhat surprising, for example, that consideration of the EGF data alone should require a substantial $k_{dp,s}$. Because our model framework considers phosphorylation in the absence of EGF, however, even explanation of data for response to EGF alone requires PTP activity at the plasma membrane.

The impact of different data used for regression was also assessed by refitting parameters excluding various data (see Table S2) or considering the various data individually (see Table S3). Excluding each type of data (e.g., EGF treatments only) individually revealed that no single treatment condition was required for the conclusion that dephosphorylation is rapid at the cell surface because each fit resulted in a $k_{dp,s}$ of ~10^0 min^{-1} (see Table S2). Fitting to data for each treatment condition individually also resulted in $k_{dp,s}$ values of at least ~10^0 min^{-1} for all cases (see Table S3). The value of $k_{dp,i}$ varied significantly among these fits, indicating that consideration of multiple types of data is required to tightly constrain this parameter.

To probe the impact of the phosphorylation-dependent endocytosis model, we substituted the more common modeling assumption that ligand-occupancy governs endocytosis. These fits also resulted in a substantial value of $k_{dp,s}$, which was greater than $k_{dp,i}$ in some cases (see Table S4). Only when we eliminated receptor phosphorylation in the absence of ligand and fit the model to data for response to ligand alone was $k_{dp,i}$ significantly larger than $k_{dp,s}$ (see Table S5). To confirm that the ligand-independent phosphorylation topology was not the only factor resulting in a $k_{dp,s} \geq k_{dp,i}$, we refit the parameters with added consideration of pulse-chase data, which resulted in a fitted $k_{dp,s} > k_{dp,i}$. (see Table S5).

Sensitivity analysis

To identify parameters that exert control over key model behaviors, we performed a sensitivity analysis for the simulation of a pulse-chase experiment and the calculation of $k_{e,e}$ for 10 ng/mL EGF (see Fig. S3). Both analyses identified parameters for EGF binding ($k_{E,fs}$ and $k_{E,rs}$), EGFR dimerization at the cell surface ($k_{d,fs}$), phosphorylation in EGF-bound dimers (k_{catE}), and $k_{dp,s}$ as important model parameters, consistent with the key roles played by EGFR phosphorylation (which is promoted by ligand binding and dimerization) and dephosphorylation at the membrane. Interestingly, the sensitivity of computing $k_{e,e}$ to changes in $k_{dp,s}$ (see Fig. S3 *A*) is consistent with the recently reported role of the receptor-like PTP DEP-1 in EGFR internalization and degradation in HeLa cells (7). Pulse-chase dynamics were also moderately sensitive to $k_{dp,i}$ (see Fig. S3 *B*). Sensitivity to $k_{dp,s}$ and $k_{dp,i}$ suggests that substantial dephosphorylation occurs before and after endocytosis for these conditions.

Predicted effects of PTP activity on ligand-mediated EGFR endocytosis

A key model assumption is that only phosphorylated receptor species are endocytosed. Because the fit suggested significant EGFR dephosphorylation at the membrane, and because $k_{e,e}$ is somewhat sensitive to changes in $k_{dp,s}$ (see Fig. S3 *A*), we used the model to predict the effect of PTP activity on the rate of EGFR endocytosis. For a range of base $k_{dp,s}$ values, S_E and $k_{e,m}$ were first computed. The values of $k_{dp,s}$ and $k_{dp,i}$ were then set to 0 min^{-1}, and $k_{e,e}$ was calculated as previously described (34). For all nominal $k_{dp,s}$ values, $k_{e,e}$ increased when PTP activity was eliminated (Fig. 5 *A*, fold change in $k_{e,e}$). The predicted effect on $k_{e,e}$ increased as the base value of $k_{dp,s}$ increased because larger $k_{e,m}$ values are required to maintain a constant base value of $k_{e,e}$ as the base $k_{dp,s}$ increases (Fig. 5 *A*, $k_{e,m}$). For the parameters in Table 1, the model predicted a modest increase in $k_{e,e}$ from the base value of 0.13 to 0.15 min^{-1} when PTP activity was eliminated.

Effects of PTP activity on EGFR inhibition

We also used the model to predict the effect of eliminating PTP activity on the inhibition of EGFR phosphorylation by gefitinib. For each scenario, $k_{e,m}$ was consistent with a $k_{e,e}$ = 0.13 min^{-1}, and the effects of 10^{-3}–10^2 μM gefitinib on EGFR phosphorylation response to 10 ng/mL EGF were predicted (Fig. 5 *B*). The inhibition curves predicted for elimination of internal or surface PTP activity were similar, with IC_{50} shifts from ~0.1 μM for the base case to ~0.3 μM for PTP elimination. The effect was slightly larger for surface-compartmentalized PTPs at higher gefitinib concentrations because EGFR internalization is impeded by gefitinib, resulting in surface-compartmentalized PTPs exerting greater influence. Elimination of all PTP activity had a much larger predicted effect (IC_{50} shift from ~0.1 to ~2 μM) due to a coupling of kinetic phenomena beyond the scope of this discussion. Overall, these results suggest that EGFR inhibitor efficacy depends heavily upon the magnitude and localization of PTP activity.

EGFR phosphate cycling

Our results suggest that EGFR tyrosines cycle between phosphorylated and unphosphorylated states more rapidly

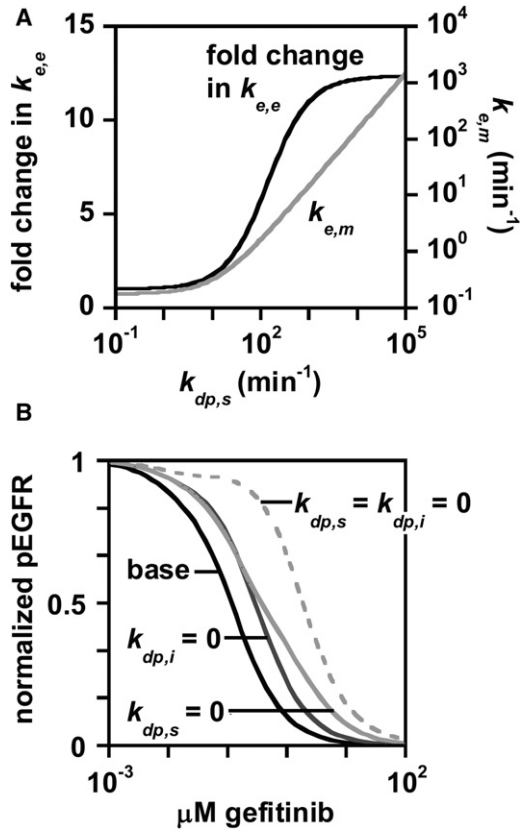

FIGURE 5 Predicted effect of dephosphorylation kinetics on EGF-mediated EGFR endocytosis and EGFR phosphorylation inhibition. (*A*) The predicted effect of eliminating all PTP activity on $k_{e,e}$ for 10 ng/mL EGF was calculated as a function of $k_{dp,s}$. Data are presented as a fold-change relative to the value of $k_{e,e}$ before elimination of PTP activity (*black line*). Corresponding $k_{e,m}$ values are also shown (*gray line*). (*B*) The effect of 5-min pretreatment with 10^{-3}–10^{2} μM gefitinib on EGFR phosphorylation response to a 20-min treatment with 10 ng/mL EGF was calculated. For each curve, model output was normalized to the pEGFR value predicted without inhibitor. Predictions were made for no change to PTP activity (base) and for elimination of PTP activity (at $t = 0$) at the plasma membrane ($k_{dp,s} = 0$), in the cell interior ($k_{dp,i} = 0$), and in both compartments ($k_{dp,s} = k_{dp,i} = 0$). For each curve, $k_{e,m}$ was chosen to be consistent with a $k_{e,e} = 0.13$ min^{-1}.

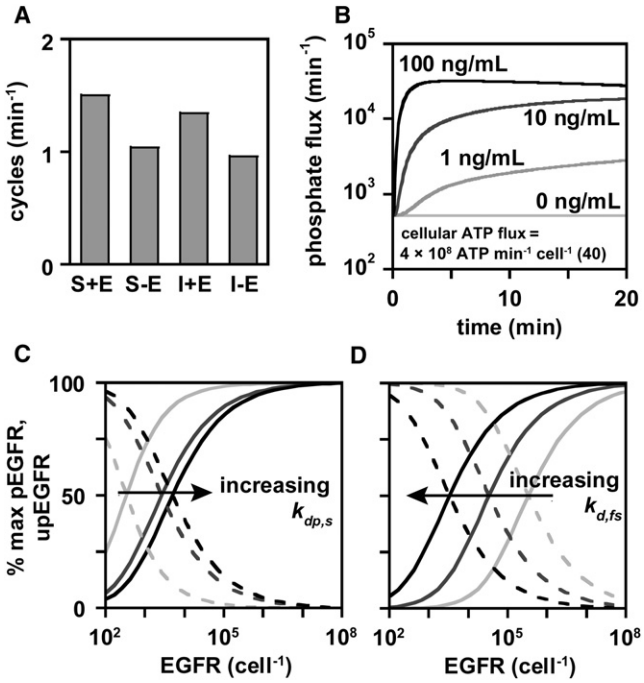

FIGURE 6 Analysis of EGFR tyrosine phosphate cycling. (*A*) Estimates of tyrosine phosphate cycling rates were made for EGF-occupied and -unoccupied EGFR at the cell surface (S+E and S−E, respectively) and for EGF-occupied and -unoccupied EGFR in the cell interior (I+E and I−E, respectively). (*B*) EGFR phosphate flux was calculated by computing the total phosphorylation rate as a function of time for treatment with 0–100 ng/mL EGF. (*C* and *D*) Steady-state phosphorylated (% max pEGFR, *solid lines*) and unphosphorylated (% max upEGFR, *dashed lines*) EGFR levels, reported as percentages of the maximum steady value for each curve, were calculated for $k_{e,m} = 0$ min^{-1}, a range of EGFR levels, 1 ng/mL EGF, and (*C*) $k_{dp,s} = 10^{-4}$, 10^{-2}, or 10^{0} min^{-1} and (*D*) $k_{d,fs} = 10^{-5}$, 10^{-4}, or 10^{-3} min^{-1}.

than is generally appreciated. This is analogous to the well-known example of phosphofructokinase and fructose-1,6-bisphosphatase and the so-called futile cycling process they mediate between fructose-6-phosphate and fructose-1,6-bisphosphate (39). The term "futile cycling" refers to a switching between states on a timescale smaller than other important process timescales. Although this cycling is more rapid than necessary for signal output magnitudes achievable with slower cycling, rapid cycling may result in key system robustness qualities (9–12). For EGFR, this cycling may also regulate receptor endocytosis and pharmacological inhibition, as we discuss.

Using the relevant phosphorylation and dephosphorylation rate constants, rates of EGFR phosphate cycling were estimated for ligand-bound and -free EGFR at the membrane and in the cell interior (Fig. 6 *A*). The estimated rate was highest (~1.5 cycles/min) for ligand-bound receptors at the cell surface because the kinetics of phosphorylation and dephosphorylation are most rapid for that scenario. We also estimated dynamic rates of ATP consumption by EGFR for four EGF concentrations (Fig. 6 *B*) and compared these to an estimate of ATP consumption for cultured cells of 4×10^8 ATP·min^{-1}·cell^{-1} (40). We thus estimated that EGFR phosphate cycling for a single tyrosine represents $\leq 0.008\%$ of cellular ATP consumption in a cell with 5×10^4 EGFR.

We also explored analogies of our results with those of the well-known study of phosphate cycling by Goldbeter and Koshland (11), who demonstrated that sensitivity to changes in reaction velocities depends upon Michaelis-Menten-like constants for phosphorylation and dephosphorylation. Whereas Goldbeter and Koshland analyzed a model where the enzyme and substrate were distinct species, EGFR is both an enzyme and a substrate, which introduces an important topological difference. In addition, PTP concentration is not specified in our model, because dephosphorylation is treated as a zeroth order process. To explore

model similarities, we varied the analog of their velocity V_1 in our model by changing EGFR expression and the analog of their dephosphorylation rate constant k_2 by changing our $k_{dp,s}$ and computed the EGFR phosphorylation response to 1 ng/mL EGF as a percent of the maximum phosphorylated EGFR level achieved for a given parameter set (Fig. 6, *C* and *D*). Consistent with the general behavior described by Goldbeter and Koshland, lowering $k_{dp,s}$ increased the sensitivity of steady EGFR phosphorylation levels to changes in EGFR level (Fig. 6 *C*). Lowering the rate constant for EGFR dimerization, an analog for lowering the a_1 parameter of Goldbeter and Koshland (11), decreased the sensitivity of steady EGFR phosphorylation levels to changes in EGFR levels (Fig. 6 *D*). EGFR phosphorylation was not sensitive to changes in the EGFR phosphorylation rate constant because the phosphorylation step is not rate-limiting for the model as described by the parameters in Table 1 (see Fig. S4).

DISCUSSION

Our results suggest that the EGFR phosphorylation dynamics we observed experimentally are consistent with timescales for EGFR dephosphorylation at the plasma membrane and in the cell interior that are smaller than the timescale for EGF-mediated EGFR endocytosis. This result stands in stark contrast to the classical view of EGFR phosphorylation dynamics wherein receptor phosphorylation occurs at the plasma membrane and dephosphorylation occurs after endocytosis. Of course, the classical view is generally consistent with the apparent timescale for receptor dephosphorylation suggested by EGFR phosphorylation in response to EGFR ligands alone. Given that most studies of EGFR phosphorylation dynamics probe response to ligands alone, it is perhaps not surprising that this classical view of receptor phosphorylation is so pervasive.

Although certain experiments in our study plainly revealed the importance of EGFR dephosphorylation at the plasma membrane (e.g., experiments with HeLa.Dyn^{K44A} cells), the incorporation of certain novel model topological features revealed the same thing when considering other data where the need for PTP activity was less obvious. For example, substantial PTP activity in the membrane compartment is required to maintain low basal levels of EGFR phosphorylation in a model that allows receptor phosphorylation in the absence of ligand to proceed as rapidly as we observed with pervanadate treatment.

The possibility that EGFR dephosphorylation may occur at different rates at the plasma membrane and in the cell interior was explored in a previous computational study (6), but the authors of that study concluded that ErbB receptor dephosphorylation occurred primarily in the cell interior for two different ErbB ligands. That study sought to qualitatively reconcile model predictions with receptor phosphorylation response to ligands only. There are also a number of topological differences between that model and ours, among them that the previous model did not consider receptor phosphorylation in the absence of ligand. All of these differences together likely explain the very different conclusion reached in that study versus the conclusions of our study.

Our implementation of a phosphorylation-dependent internalization model (which has been used in at least one previous study (21)), instead of a ligand occupancy model as in other studies (6,19,20), is well supported by experimental data, as reviewed by Sorkin and Goh (1). For example, mutation of key EGFR tyrosines reduced EGF-mediated EGFR internalization rates in mouse fibroblasts, suggesting that tyrosine phosphorylation is indeed required for efficient ligand-mediated EGFR endocytosis (1). It should also be emphasized, however, that our particular implementation of phosphorylation-dependent receptor internalization is novel, to the best of our knowledge. Specifically, our iterative calculation of $k_{e,m}$ values that lead to optimum model matching of experimentally reported $k_{e,e}$ values is an important and, we believe, unique way in which our model recapitulates experimental data.

Because our studies concluded that substantial EGFR dephosphorylation occurs at the plasma membrane, and because we have implemented a phosphorylation-dependent model for EGFR endocytosis, it was not surprising that the model predicted that PTP activity at the plasma membrane may impede EGFR endocytosis (Fig. 5 *A*). Interestingly, this model-predicted effect is qualitatively consistent with the apparent effect of knockdown of the receptor-like PTP DEP-1 on EGFR internalization observed recently in HeLa cells (7). We applied our model to estimate that Tarcic et al. (7) observed a decrease in surface-localized EGFR in response to EGF consistent with $k_{e,e} = 0.2\ \text{min}^{-1}$ in their flow cytometry data for control cells and a threefold increase in $k_{e,e}$ with DEP-1 knockdown. Assuming DEP-1 accounts for all PTP activity at the plasma membrane, our model predicts a threefold increase in $k_{e,e}$ with a $k_{dp,s}$ ~$3 \times 10^1\ \text{min}^{-1}$ (Fig. 5 *A*), which is significantly larger than the best fit $k_{dp,s}$ (Table 1). Of course, our model results represent the predicted effect of instantaneous inhibition of PTP activity. It is possible that knockdown of DEP-1 resulted in an adaptive response that amplified the effect of DEP-1 knockdown in the experiments of Tarcic et al. (7). In addition, it is possible that the tendency of at least some EGFR antibodies to not efficiently recognize pEGFR (noted in the Supporting Material) resulted in an effect on EGFR levels that was more apparent than real in the data of Tarcic et al. (7).

Our model results regarding PTP activity at the plasma membrane were directly tested through comparison of model predictions with pulse-chase experiments in HeLa.Dyn^{K44A} cells. Although the model parameters fitted through consideration of parental HeLa cell data only did a reasonable job

of predicting the rate at which plasma-membrane-sequestered receptors were dephosphorylated, consideration of the HeLa.Dyn^{K44A} cell data in a refitting of the model aided in refining our parameter estimates. In the future, it will be interesting and important to also directly test other model predictions (e.g., the effects of PTP inhibition on EGFR pharmacological inhibition) and to use such results to refine the model in a similar way. Another particularly important aspect of the biochemistry we investigated that would be important to understand more deeply is the extent to which PTP activity, with respect to EGFR, is time-dependent for the various cell treatment conditions utilized in our study. Surprisingly, very little has been reported on this subject. As far as we are aware, only changes in the activity of the cytosolic PTP SHP2 in response to ligands including EGF have been studied in any detail (41).

Although our study focuses on receptor-level regulation, phosphatases have been considered in some models of signaling processes distal to receptors. For example, the models developed by Heinrich et al. (12) for generalized linear signaling cascades demonstrated the role of phosphatases in setting the amplitude, duration, and amplification of signaling responses to upstream changes in receptor activation. Our model similarly points to a key role for PTPs in determining EGFR phosphorylation amplitude and duration. Importantly, this regulation is revealed by our model to occur on a timescale that is smaller than that for other important process timescales, including the typical timescale for complete activation of MAP kinase cascades and receptor trafficking. Incorporation of these receptor-level considerations revealed by our study in models including downstream cascades may help to more fully recapitulate dynamic signaling data that spans the space from the receptor to key downstream-signaling intermediates.

SUPPORTING MATERIAL

Experimental methods, four figures, five tables, and three references are available at http://www.biophysj.org/biophysj/supplemental/S0006-3495(12)00378-5.

We thank Mark Lemmon, Ravi Radhakrishnan, Alexander Sorkin, Matt Flamm, and Jeremy Purvis for helpful discussions, and Sandra Schmid for providing HeLa cells with conditional expression of wild-type or K44A dynamin.

This work was supported in part by grant IRG-78-002-30 from the American Cancer Society, by the University of Pennsylvania Training Program in Cancer Pharmacology (R25 CA101871-07), and by laboratory startup funds from the University of Pennsylvania.

REFERENCES

1. Sorkin, A., and L. K. Goh. 2009. Endocytosis and intracellular trafficking of ErbBs. *Exp. Cell Res.* 315:683–696.
2. Tiganis, T. 2002. Protein tyrosine phosphatases: dephosphorylating the epidermal growth factor receptor. *IUBMB Life.* 53:3–14.
3. Knight, Z. A., and K. M. Shokat. 2005. Features of selective kinase inhibitors. *Chem. Biol.* 12:621–637.
4. Kholodenko, B. N., O. V. Demin, …, J. B. Hoek. 1999. Quantification of short term signaling by the epidermal growth factor receptor. *J. Biol. Chem.* 274:30169–30181.
5. Schoeberl, B., E. A. Pace, …, U. B. Nielsen. 2009. Therapeutically targeting ErbB3: a key node in ligand-induced activation of the ErbB receptor-PI3K axis. *Sci. Signal.* 2:ra31.
6. Hendriks, B. S., J. Cook, …, D. de Graaf. 2006. Computational modeling of ErbB family phosphorylation dynamics in response to transforming growth factor α and heregulin indicates spatial compartmentation of phosphatase activity. *Syst. Biol. (Stevenage).* 153:22–33.
7. Tarcic, G., S. K. Boguslavsky, …, Y. Yarden. 2009. An unbiased screen identifies DEP-1 tumor suppressor as a phosphatase controlling EGFR endocytosis. *Curr. Biol.* 19:1788–1798.
8. Haj, F. G., B. Markova, …, B. G. Neel. 2003. Regulation of receptor tyrosine kinase signaling by protein tyrosine phosphatase-1B. *J. Biol. Chem.* 278:739–744.
9. Gomez-Uribe, C., G. C. Verghese, and L. A. Mirny. 2007. Operating regimes of signaling cycles: statics, dynamics, and noise filtering. *PLoS Comput. Biol.* 3:e246.
10. Qian, H., and D. A. Beard. 2006. Metabolic futile cycles and their functions: a systems analysis of energy and control. *Syst. Biol. (Stevenage).* 153:192–200.
11. Goldbeter, A., and D. E. Koshland, Jr. 1981. An amplified sensitivity arising from covalent modification in biological systems. *Proc. Natl. Acad. Sci. USA.* 78:6840–6844.
12. Heinrich, R., B. G. Neel, and T. A. Rapoport. 2002. Mathematical models of protein kinase signal transduction. *Mol. Cell.* 9:957–970.
13. Schaapveld, R., B. Wieringa, and W. Hendriks. 1997. Receptor-like protein tyrosine phosphatases: alike and yet so different. *Mol. Biol. Rep.* 24:247–262.
14. Tenev, T., S. A. Böhmer, …, F. D. Böhmer. 2000. Perinuclear localization of the protein-tyrosine phosphatase SHP-1 and inhibition of epidermal growth factor-stimulated STAT1/3 activation in A431 cells. *Eur. J. Cell Biol.* 79:261–271.
15. Frangioni, J. V., P. H. Beahm, …, B. G. Neel. 1992. The nontransmembrane tyrosine phosphatase PTP-1B localizes to the endoplasmic reticulum via its 35 amino acid C-terminal sequence. *Cell.* 68:545–560.
16. Bourdeau, A., N. Dubé, and M. L. Tremblay. 2005. Cytoplasmic protein tyrosine phosphatases, regulation and function: the roles of PTP1B and TC-PTP. *Curr. Opin. Cell Biol.* 17:203–209.
17. Källström, H., A. Lindqvist, …, C. K. Rosenthal. 2005. Cdc25A localization and shuttling: characterization of sequences mediating nuclear export and import. *Exp. Cell Res.* 303:89–100.
18. Haj, F. G., P. J. Verveer, …, P. I. Bastiaens. 2002. Imaging sites of receptor dephosphorylation by PTP1B on the surface of the endoplasmic reticulum. *Science.* 295:1708–1711.
19. Hendriks, B. S., L. K. Opresko, …, D. Lauffenburger. 2003. Coregulation of epidermal growth factor receptor/human epidermal growth factor receptor 2 (HER2) levels and locations: quantitative analysis of HER2 overexpression effects. *Cancer Res.* 63:1130–1137.
20. Hendriks, B. S., L. K. Opresko, …, D. Lauffenburger. 2003. Quantitative analysis of HER2-mediated effects on HER2 and epidermal growth factor receptor endocytosis: distribution of homo- and heterodimers depends on relative HER2 levels. *J. Biol. Chem.* 278:23343–23351.
21. Schoeberl, B., C. Eichler-Jonsson, …, G. Müller. 2002. Computational modeling of the dynamics of the MAP kinase cascade activated by surface and internalized EGF receptors. *Nat. Biotechnol.* 20:370–375.
22. Purvis, J., V. Ilango, and R. Radhakrishnan. 2008. Role of network branching in eliciting differential short-term signaling responses in the hypersensitive epidermal growth factor receptor mutants implicated in lung cancer. *Biotechnol. Prog.* 24:540–553.

23. French, A. R., D. K. Tadaki, …, D. A. Lauffenburger. 1995. Intracellular trafficking of epidermal growth factor family ligands is directly influenced by the pH sensitivity of the receptor/ligand interaction. *J. Biol. Chem.* 270:4334–4340.

24. Hubley, M. J., R. C. Rosanske, and T. S. Moerland. 1995. Diffusion coefficients of ATP and creatine phosphate in isolated muscle: pulsed gradient ^{31}P NMR of small biological samples. *NMR Biomed.* 8:72–78.

25. Lauffenburger, D., and J. Linderman. 1996. Receptors: Models for Binding, Trafficking, and Signaling. Oxford University Press, New York.

26. Wakeling, A. E., S. P. Guy, …, K. H. Gibson. 2002. ZD1839 (Iressa): an orally active inhibitor of epidermal growth factor signaling with potential for cancer therapy. *Cancer Res.* 62:5749–5754.

27. Zamaraeva, M. V., R. Z. Sabirov, …, Y. Okada. 2005. Cells die with increased cytosolic ATP during apoptosis: a bioluminescence study with intracellular luciferase. *Cell Death Differ.* 12:1390–1397.

28. Pedersen, M. W., N. Pedersen, …, H. S. Poulsen. 2005. Differential response to gefitinib of cells expressing normal EGFR and the mutant EGFRvIII. *Br. J. Cancer.* 93:915–923.

29. Ganley, I. G., K. Carroll, …, S. Pfeffer. 2004. Rab9 GTPase regulates late endosome size and requires effector interaction for its stability. *Mol. Biol. Cell.* 15:5420–5430.

30. Zhou, M., S. Felder, …, J. Schlessinger. 1993. Real-time measurements of kinetics of EGF binding to soluble EGF receptor monomers and dimers support the dimerization model for receptor activation. *Biochemistry.* 32:8193–8198.

31. Fan, Y. X., L. Wong, …, G. R. Johnson. 2004. Ligand regulates epidermal growth factor receptor kinase specificity: activation increases preference for GAB1 and SHC versus autophosphorylation sites. *J. Biol. Chem.* 279:38143–38150.

32. Doody, J. F., Y. Wang, …, Y. R. Hadari. 2007. Inhibitory activity of cetuximab on epidermal growth factor receptor mutations in non small cell lung cancers. *Mol. Cancer Ther.* 6:2642–2651.

33. Ciaccio, M. F., J. P. Wagner, …, R. B. Jones. 2010. Systems analysis of EGF receptor signaling dynamics with microwestern arrays. *Nat. Methods.* 7:148–155.

34. Lund, K. A., L. K. Opresko, …, H. S. Wiley. 1990. Quantitative analysis of the endocytic system involved in hormone-induced receptor internalization. *J. Biol. Chem.* 265:15713–15723.

35. Lazzara, M. J., K. Lane, …, D. A. Lauffenburger. 2010. Impaired SHP2-mediated extracellular signal-regulated kinase activation contributes to gefitinib sensitivity of lung cancer cells with epidermal growth factor receptor-activating mutations. *Cancer Res.* 70:3843–3850.

36. Berkers, J. A., P. M. van Bergen en Henegouwen, and J. Boonstra. 1991. Three classes of epidermal growth factor receptors on HeLa cells. *J. Biol. Chem.* 266:922–927.

37. Schmidt, H., and M. Jirstrand. 2006. Systems Biology Toolbox for MATLAB: a computational platform for research in systems biology. *Bioinformatics.* 22:514–515.

38. Offterdinger, M., V. Georget, …, P. I. Bastiaens. 2004. Imaging phosphorylation dynamics of the epidermal growth factor receptor. *J. Biol. Chem.* 279:36972–36981.

39. Sel'kov, E. E., N. V. Avseenko, and I. Kirsta. 1979. [Allosteric regulation in the open futile cycle fructose-6-P-fructose-1,6-P2]. *Biofizika.* 24:829–835.

40. Buttgereit, F., and M. D. Brand. 1995. A hierarchy of ATP-consuming processes in mammalian cells. *Biochem. J.* 312:163–167.

41. Araki, T., H. Nawa, and B. G. Neel. 2003. Tyrosyl phosphorylation of Shp2 is required for normal ERK activation in response to some, but not all, growth factors. *J. Biol. Chem.* 278:41677–41684.